

Time-resolved photoemission spectroscopy of electronic cooling and localization in $\text{CH}_3\text{NH}_3\text{PbI}_3$ crystals

Zhesheng Chen,¹ Min-i Lee,² Zailan Zhang,³ Hiba Diab,⁴ Damien Garrot,⁵ Ferdinand Lédée,^{4,6} Pierre Fertey,⁷ Evangelos Papalazarou,² Marino Marsi,² Carlito Ponseca,⁸ Emmanuelle Deleporte,^{4,6} Antonio Tejada,² and Luca Perfetti¹

¹Laboratoire des Solides Irradiés, Ecole Polytechnique, CNRS, CEA, Université Paris-Saclay, 91128 Palaiseau Cedex, France

²Laboratoire de Physique des Solides, CNRS, Université Paris-Saclay, Université Paris-Sud, 91405 Orsay, France

³Institut de Minéralogie et de Physique des Matériaux et de Cosmochimie (IMPMC), UMR CNRS 7590, Université Pierre et Marie Curie - Case 115, 4, Place Jussieu, 75252 Paris Cedex 05, France

⁴Laboratoire Aimé Cotton, Ecole Normale Supérieure ENS Paris-Saclay, CNRS, Université Paris-Sud, Université Paris-Saclay, 91405 Orsay, France

⁵Groupe d'Etudes de la Matière Condensée (GEMaC), CNRS, Université de Versailles, Saint-Quentin-en-Yvelines, Université Paris-Saclay, 45 Avenue des Etats-Unis, 78035 Versailles Cedex, France

⁶Laboratoire de Photophysique et Photochimie Supramoléculaires et Macromoléculaires de l'Ecole Normale Supérieure de Cachan, 61 Avenue du Président Wilson, 94235 Cachan, France

⁷Société Civile Synchrotron SOLEIL, L'Orme des Merisiers, Saint-Aubin - BP 48, 91192 Gif-sur-Yvette, France

⁸Division of Chemical Physics, Lund University, Box 124, 221 00 Lund, Sweden

(Received 21 April 2017; published 26 September 2017)

We measure the surface of $\text{CH}_3\text{NH}_3\text{PbI}_3$ single crystals by making use of two-photon photoemission spectroscopy. Our method monitors the electronic distribution of photoexcited electrons, explicitly discriminating the initial thermalization from slower dynamical processes. The reported results disclose the fast-dissipation channels of hot carriers (0.25 ps), set an upper bound to the surface-induced recombination velocity (<4000 cm/s), and reveal the dramatic effect of shallow traps on the electrons dynamics. The picosecond localization of excited electrons in degraded $\text{CH}_3\text{NH}_3\text{PbI}_3$ samples is consistent with the progressive reduction of photoconversion efficiency in operating devices. Minimizing the density of shallow traps and solving the aging problem may boost the macroscopic efficiency of solar cells to the theoretical limit.

DOI: [10.1103/PhysRevMaterials.1.045402](https://doi.org/10.1103/PhysRevMaterials.1.045402)

I. INTRODUCTION

Hybrid metal-organic perovskite semiconductors such as methylammonium lead iodide $\text{CH}_3\text{NH}_3\text{PbI}_3$ (MAPbI_3) have emerged as promising new materials for photovoltaic devices and optoelectronics. The power conversion efficiency of solar cells based on perovskite materials exceeded 20% within eight years [1–3] and a theoretical limit of 30% has been proposed [4]. Such an impressive performance results from favorable material properties such as a direct band gap of roughly 1.6 eV, a large absorption coefficient, and high charge carrier mobility [5].

The perovskite materials can be broadly divided into two types: bulk crystals and polycrystalline thin films. Single crystals of MAPbI_3 have long electron-hole diffusion length (up to 175 μm) and low density of recombination centers [6–8]. Thin films are more suitable for device application but display photoexcited carriers with smaller mobility and shorter lifetime [9–11]. Moreover, the fast degradation of thin films in operating conditions poses serious limits to viable applications. Both the photoexposure and annealing in atmospheric conditions induce the formation of PbI_2 inclusions [12]. The main objective of our work is to show that compositional disorder leads to shallow traps where carriers localize on the picosecond time scale.

The carrier diffusion, localization, and recombination are investigated by two-photon photoemission (2PPE) experiments on single MAPbI_3 crystals. Remarkably, 2PPE monitors the energy distribution of excited electrons with good temporal resolution and high surface sensitivity. Moreover, the clean

surface of a single crystal is a model and well-controlled system with which to explore the impact of localized states on the electronic motion.

The article is organized as follows: Section II contains x-ray diffraction, photoluminescence, and photoemission characterization of our crystals. Section III describes the methodology and the technical aspects of the 2PPE technique. Section IV discusses the subpicosecond cooling of excited electrons. Section V proposes a diffusion model to explain the observed evolution of the 2PPE signal. Section VI investigates the carrier localization in intentionally degraded crystals. Section VII deals with carrier recombination and possible effects of the surface. Section VIII reports the conclusions.

II. SAMPLE CHARACTERIZATION

We investigate single crystals of MAPbI_3 grown by the inverse crystallization method. Methylammonium iodide (0.78 g, 5 mmol) and lead iodide (2.30 g, 5 mmol) were dissolved in γ -butyrolactone (5 mL) at 60 °C. The yellow solution (2 mL) was placed in a vial and heated at 120 °C during one to four hours depending on the desired crystal size. As shown in the scanning electron microscope image of Fig. 1(a), the samples are crystals of millimetric size. X-ray diffraction measurements have been performed at the CRISTAL beamline of synchrotron SOLEIL by means of a four-circle diffractometer. The Bragg reflections in Fig. 1(b) confirm the high quality of the single crystals [13].

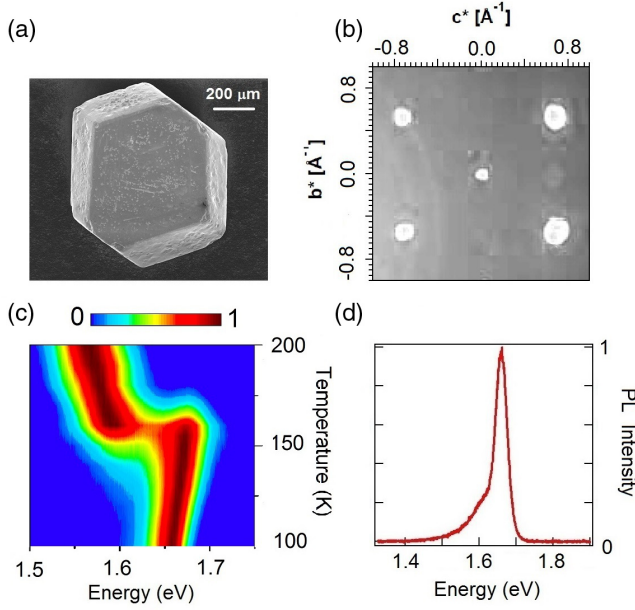


FIG. 1. (a) Image of a single MAPbI₃ crystal acquired by scanning electron microscope. (b) X-ray diffraction of Bragg peaks in the $\{0, k_{\perp}, k_{\parallel}\}$ plane of the tetragonal phase. (c) Intensity map of photoluminescence as function of photon energy and sample temperature. The abrupt transition around 160 K is due to the tetragonal to orthorhombic phase transition. (d) Photoluminescence spectrum of MAPbI₃ measured at 130 K.

Figure 1(c) displays the photoluminescence map of the MAPbI₃ single crystals between 100 K and 200 K. The emission is composed of a single peak arising from electron-hole recombination across the band gap. Upon cooling, the sudden blueshift of the emission line at $\cong 160$ K [14] is due to the widening of the band gap at the tetragonal to orthorhombic phase transition. Below 160 K, the evolution of photoluminescence with temperature indicates a reduction of the band gap with lattice contraction. From the photoluminescence spectrum recorded at 130 K [see Fig. 1(d)], we extract the band gap energy $\Delta_g = 1.66$ eV. In the following, we will refer all spectroscopic measurements to the orthorhombic phase at 130 K.

Single crystals have been mounted on the $\{0, 1, 0\}$ plane and cleaved in ultrahigh vacuum at base pressure below 10^{-10} mbar. Despite the high crystalline quality of our samples, low-energy electron diffraction (LEED) did not display any Bragg spot. We argue that cleaved surfaces are rough, probably because of the brittle nature of MAPbI₃. Figure 2(a) shows angle-resolved photoelectron spectroscopy (ARPES) measurements performed at the CASSIOPEE beamline of synchrotron SOLEIL. The selected photon beam of 94 eV maximizes the cross section of the valence band and corresponds to a perpendicular wave vector $k_{\perp} \sim 0$. Variations of spectral intensity with respect to k_{\parallel} are consistent with the electronic band dispersion in the first Brillouin zone [13]. We show in Fig. 2(b) the spectrum obtained by integrating the photoelectron map in the interval $[-1.5, 1.5] \text{ \AA}^{-1}$. The chemical potential μ_F is located 1.6 eV higher than the top of the valence band, indicating that MAPbI₃ crystals are naturally *n* doped.

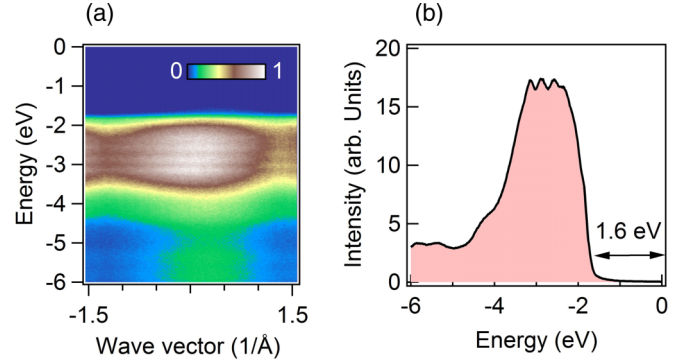


FIG. 2. (a) Photoelectron intensity map acquired with photon energy of 94 eV in the $\{k_{\parallel}, k_{\perp} \sim 0, 0\}$ direction of the tetragonal phase. (b) Wave-vector-integrated photoelectron spectrum acquired with photon energy of 94 eV. The maximum of the valence band is located 1.6 eV below the chemical potential.

III. TWO-PHOTON PHOTOEMISSION

The temporal evolution of the excited state is measured by means of two-photon photoemission (2PPE). Our photon source is a Ti:sapphire laser system delivering 6 μJ pulses with a repetition rate of 250 kHz. Part of the fundamental beam ($h\nu_0 = 1.55$ eV) is converted to the second harmonic ($h\nu_1 = 3.15$ eV) in a β -BBO crystal while the rest is employed to generate the third harmonic ($h\nu_2 = 4.7$ eV) [15]. We photoexcite the sample at 130 K by 50 fs pump pulses of 20 $\mu\text{J}/\text{cm}^2$, centered at $h\nu_1$. According to the reported value of the absorption coefficient [16], this pulse results in an electron-hole density of $8 \times 10^{18} \text{ cm}^{-3}$.

As shown in Fig. 3(a) the photons of the pump beam generate photoexcited electrons with excess energy up to $h\nu_1 - \Delta_g = 1.5$ eV, thereby inducing optical transitions in two branches of the conduction band. After a variable delay time, probe pulses centered at $h\nu_2 = 4.7$ eV promote the excited electrons above the vacuum level [see Fig. 3(b)]. Photoelectrons outgoing from the sample are detected by a hemispherical energy analyzer with an acceptance angle of roughly $5 \times 1 \text{ deg}^2$ around normal emission. The overall energy resolution of 60 meV is dominated by the bandwidth of the probe beam. This technique provides a direct mapping of the electronic distribution in the photoexcited sample. Moreover, the electrons that have absorbed the two photons hold an inelastic mean-free path of a few nanometers [17]. Such high surface sensitivity can be exploited to question the electron dynamics in the topmost layers of the cleaved crystal.

IV. ULTRAFAST COOLING OF HOT ELECTRONS

We show in Fig. 4(a) a color scale plot of the photoelectron intensity acquired as a function of kinetic energy and pump-probe delay. The nominal kinetic energy of the conduction band minimum is $E_c = h\nu_2 - \phi + \Delta_g - \mu_F + E_v = 0.45$ eV, where $\phi = 4.3$ eV is the work function of our analyzer. As shown in Fig. 4(b), the spectrum acquired at the maximal overlap between pump and probe pulse (zero delay) displays a peak in proximity of E_c , a second peak near $E' = E_c + 0.35$ eV, and a third peak at $E'' = E_c + 0.9$ eV. As sketched in Fig. 3(a), the structures E' and E'' are located

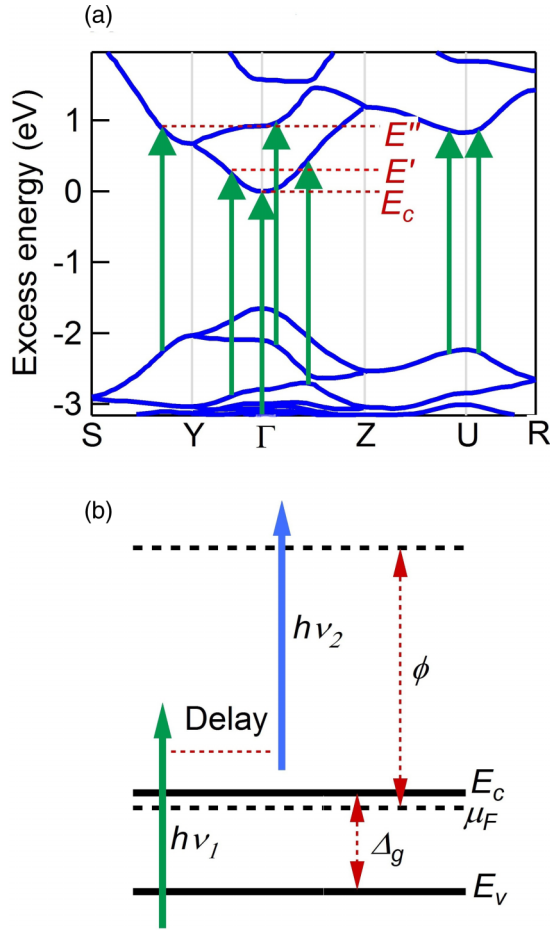


FIG. 3. (a) Band structure of MAPbI₃ freely adapted from Filip *et al.* [18]. The green arrows stand for direct transitions induced by photons with $h\nu_1 = 3.15$ eV. (b) Energetics of the 2PPE experiment with pump photon energy $h\nu_1$, probe photon energy $h\nu_2$, band gap Δ_g , chemical potential μ_F , and analyzer work function ϕ .

at excess energies where the 3.15 eV photons generate high density of optical transitions [18].

Next, we consider the dynamics of the electrons soon after the arrival of the pump pulse. Figure 4(b) shows that the excited electronic distribution varies strongly within the first picosecond. The electrons with large excess energy thermalize towards the bottom of the conduction band by means of electron-electron scattering and phonon emission. We exclude the occurrence of carrier multiplication because the photon energy of the pump beam is lower than twice the value of the band gap. The initial thermalization time can be quantified by evaluating the average kinetic energy contained in the spectrum as a function of time. In practice, we calculate $\langle E \rangle_t = \int I(E,t)E dE / \int I(E,t) dE$, where E is the kinetic energy, $I(E,t)$ is the photoelectron intensity, and t is the pump-probe delay.

Figure 4(c) shows the resulting $\langle E \rangle_t$, together with the fit by an exponential decay with a time constant of $\tau_1 = 0.25$ ps. This value is in excellent agreement with recent 2PPE experiments on MAPbI₃ thin films [19] and it is faster than the energy relaxation time observed in inorganic semiconductors [20]. We suggest that the rapid electronic cooling of MAPbI₃ arises

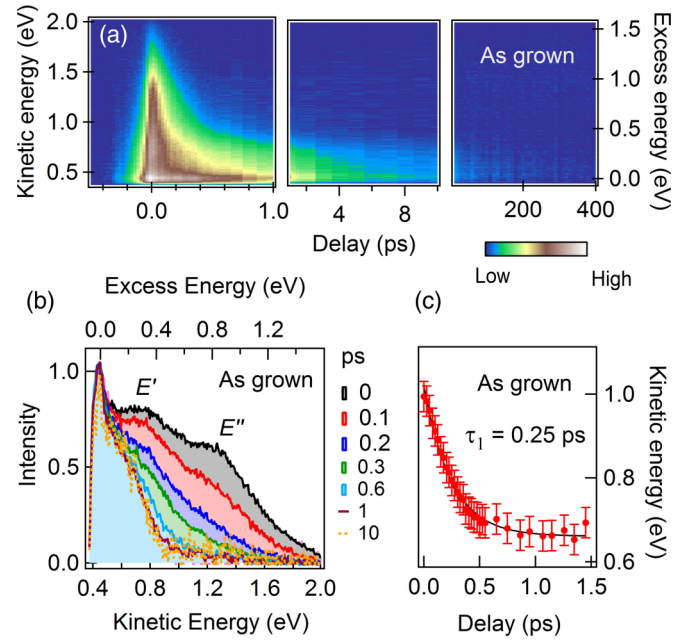


FIG. 4. (a) Photoelectron intensity map in the as-grown sample as a function of kinetic energy and pump-probe delay. (b) Energy distribution curves acquired at different values of the pump-probe delay and normalized to their maximum value. (c) Evolution of the average kinetic energy as a function of time. The solid line is an exponential fit with time constant $\tau_1 = 0.25$ ps.

via the coupling of excited carriers to the internal vibrations of the CH₃NH₃⁺ cations. For example, the stretching modes of C-H and N-H bonds hold quantum energy of 370–400 meV and can efficiently drain the excess energy of photoexcited electrons [21]. Moreover, the recent observation of optical sidebands in two-dimensional hybrid perovskites indicates a sizable coupling of the exciton to an organic mode with quantum energy of 40 meV [22].

According to Fig. 4(c), the hot electrons will reach quasiequilibrium with the coupled phonons after $\cong 3\tau_1 = 0.75$ ps. Several authors suggest that strongly coupled modes attain an occupation level higher than the thermal one and relax on the slower time scale of anharmonic interaction [23,24]. In this respect, time-resolved Raman experiments may be helpful to address the specific vibrational modes where electrons transfer their excess energy [25]. Note in Fig. 4(b) that the spectra acquired at delay times of 1 ps and 10 ps display a shoulder at excess energy ~ 0.2 eV. Niesner *et al.* observed a similar shoulder only in the tetragonal phase of MAPbI₃ and they ascribed it to an unconventional kind of polaronic dressing [19,26]. This issue requires additional measurements and it is currently under investigation.

V. DIFFUSION IN THE AS-GROWN SAMPLE

Since the 2PPE technique probes carriers within the topmost nanometers, the integrated signal $\int I(E,t) dE$ follows the instantaneous electronic concentration at the surface of the sample times the photoemission cross section. Once the electrons have fully thermalized, the photoemission cross section becomes time independent. Therefore, the progressive

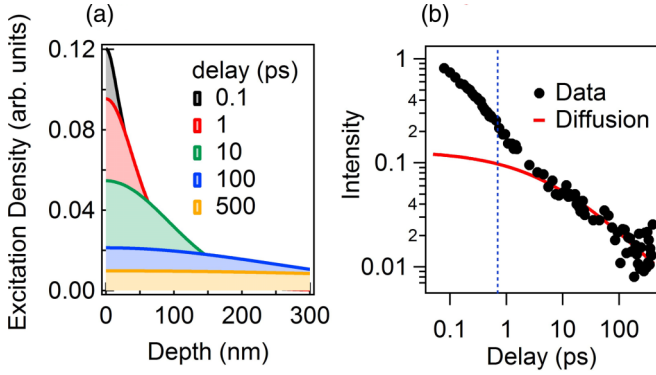


FIG. 5. (a) The density profile of photoexcited electrons is calculated by the diffusion model of Eq. (1) for selected delay times. (b) The integrated intensity of the 2PPE signal (black marks) as a function of time is compared with the diffusion model (red line). The dotted blue line at $t = 3\tau_1$ indicates the delay time when electrons have fully thermalized.

decay of the 2PPE signal that can be observed in the middle and right panels of Fig. 4(a) is due to the drift-diffusion of electronic charges from the surface into the bulk. First, we analyze the effect of pure diffusion on the long-time-scale dynamics. Electrons that are excited in an optical penetration depth [16] $\alpha^{-1} = 50$ nm move in to the bulk because of Brownian motion. The electronic concentration at distance x from the surface and pump-probe delay t is given by [27]

$$n(x,t) \propto \frac{1}{2} \exp\left(-\frac{x^2}{4Dt}\right) w\left(\alpha\sqrt{Dt} - \frac{x}{2\sqrt{Dt}}\right) + \frac{1}{2} \exp\left(-\frac{x^2}{4Dt}\right) w\left(\alpha\sqrt{Dt} + \frac{x}{2\sqrt{Dt}}\right), \quad (1)$$

where $w(z) = \exp(z^2)[1 - \text{erf}(z)]$ and D is the electron diffusion constant of MAPbI₃ crystals at 130 K. We recall that the mobility μ of MAPbI₃ is limited by electron-phonon scattering [11] and scales as $T^{-3/2}$. Therefore, we can invoke the Einstein relation $D = \mu k_b T \propto T^{-1/2}$ and refer to the literature value of D at room temperature [6] in order to estimate the electron diffusion constant at $T = 130$ K. The resulting $D = 3$ cm²/s is plugged into Eq. (1) of the electronic density. We show in Fig. 5(a) the resulting $n(x,t)$ as a function of x for selected values of t . Figure 5(b) compares the calculated $n(0,t)$ with the experimental evolution of the photoemission signal in the temporal window [0.05, 400] ps. The measured decay follows the diffusion behavior for delay time larger than 3 ps but proceeds much faster during the first picosecond. Niesner *et al.* ascribed this initial drop to the rapid variation of the photoemission cross section during the thermalization process [19]. On one hand, it is fully plausible that carriers changing energy and wave vector display sudden changes of cross section. On the other hand, the measured intensity deviates from the diffusion model even after the electrons have fully thermalized (namely for $3\tau_1 < t < 10\tau_1$). Eventually, built-in fields at the sample surface lead to an initial drift of the electrons out of the detection regions. Such ultrafast segregation between electrons and holes has been recently observed in other doped semiconductors [28]. In the case

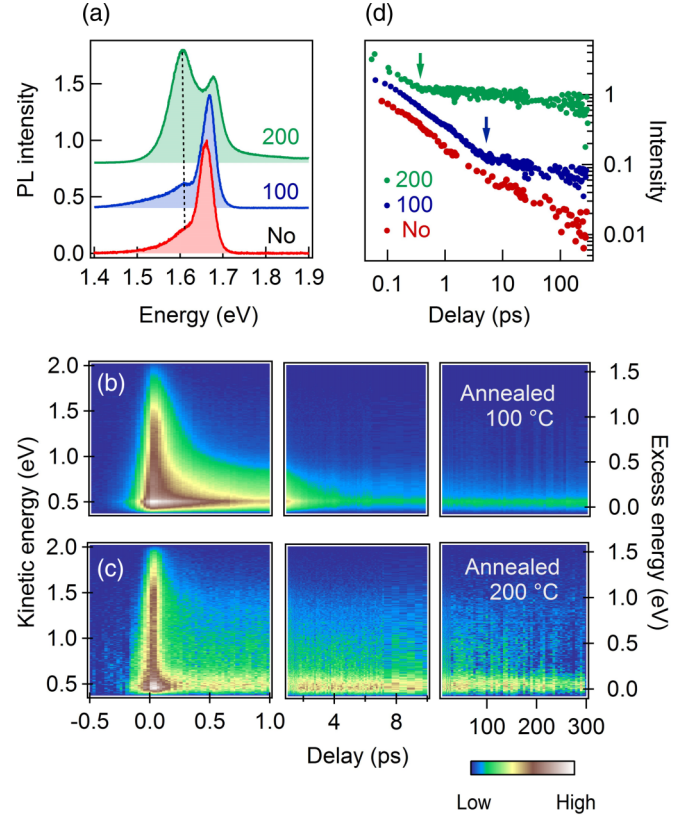


FIG. 6. (a) Photoluminescence spectra acquired as grown, 100 °C annealed, and 200 °C samples. The dashed line is a guide to the eye showing the development of trapped states upon annealing. Photoelectron intensity map in samples annealed at 100 °C (b) and 200 °C (c). (d) Temporal evolution of the integrated 2PPE signal in the pristine and annealed samples. The arrows indicate characteristic time scale when electronic trapping takes place.

of MAPbI₃ the built-in field may originate from the residual polarity of the crystal termination [29].

VI. ELECTRONIC LOCALIZATION IN ANNEALED SAMPLES

After having discussed the drift diffusion of the electrons in high-quality crystals, we can address the important role that sample degradation has on the carrier motion. The data of the as-grown crystal are compared with the ones of the samples annealed in air at 100 °C (MA100) and 200 °C (MA200) for 30 minutes. The MAPbI₃ single crystal is very sensitive to humidity, illumination, and annealing temperature. Figure 6(a) shows photoluminescence on the as-grown and annealed samples. Upon increasing the annealing temperature, a new photoluminescence peak, arising from trapped states, develops $\cong 60$ meV below the band-gap value. We report in Figs. 6(b) and 6(c) the photoelectron intensity map acquired on annealed samples as a function of pump-probe delay. The MA100 and the as-grown sample display similar behavior on the short time scale ($\cong 1$ ps). However the 2PPE map of MA100 [Fig. 6(b)] and MA200 [Fig. 6(c)] holds a remnant signal lasting longer than 300 ps. We argue that shallow traps introduced by annealing lead to a partial localization of the electrons. Note in Fig. 6(d) that the long-time-scale

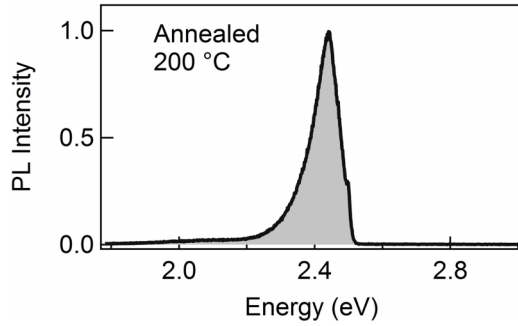


FIG. 7. Photoluminescence emitted in the visible spectral range from the MA200 sample at 10 K. The peak centered at 2.45 eV arises from carrier recombination in PbI_2 inclusions.

evolution of the integrated 2PPE signal deviates from the diffusive $1/\sqrt{t}$ decay only in the case of annealed samples. The onset of the trapping strongly depends on the quality of the crystal. In MA100 the localization takes place on the time scale of a few picoseconds whereas it falls below the picosecond in highly degraded MA200. Probably the defect density of MA200 is so high that localization takes place as soon as the electrons cool down below the mobility edge of the traps. The localization landscape of conduction electrons is related to the compositional disorder of degraded samples [12]. According to Xie *et al.*, an annealing to 150 °C leads to a shallow distribution of I and Pb components in the MAPbI_3 thin film [30]. Furthermore, Deretzis *et al.* reported that thermodynamic degradation above 150 °C can induce a partial conversion of MAPbI_3 into PbI_2 [31]. The low-temperature photoluminescence measurements in Fig. 7 confirm that MA200 contains large inclusions of PbI_2 .

VII. RADIATIVE AND SURFACE RECOMBINATION

Remarkably, the long-lasting presence of electrons at the surface of MA100 and MA200 indicates a long recombination time of the photoexcited carriers. It has been shown that direct recombination between electrons and holes [10] becomes dominant at photoexcitation density $\sim 10^8 \text{ cm}^{-3}$. We display in Fig. 8 the fitting curve obtained by a kinetic equation with bimolecular recombination rate $\gamma = 4 \pm 1 \times 10^{-10} \text{ cm}^3/\text{s}$. The extracted value is in good agreement with previous reports and defies the Langevin prediction by four orders of magnitude [10]. Wehrenfennig *et al.* proposed that electrons and holes are preferentially localized in spatially distinct regions of the disordered landscape. Accordingly, density functional calculations on MaPbI_3 predict that valence band maxima consist of 6s and 5p orbitals of lead and iodine, respectively, while conduction band minima mostly incorporate 6p orbitals of lead [32].

Next, we exploit the high surface sensitivity of 2PPE to question the surface recombination velocity of samples cleaved in ultrahigh-vacuum conditions. By following the literature [27,33], we model the density of the electrons at the surface as

$$n(0,t) \propto \frac{\alpha D_T w(\alpha \sqrt{D_T t}) - S w\left(S \sqrt{\frac{t}{D_T}}\right)}{\alpha D_T - S}, \quad (2)$$

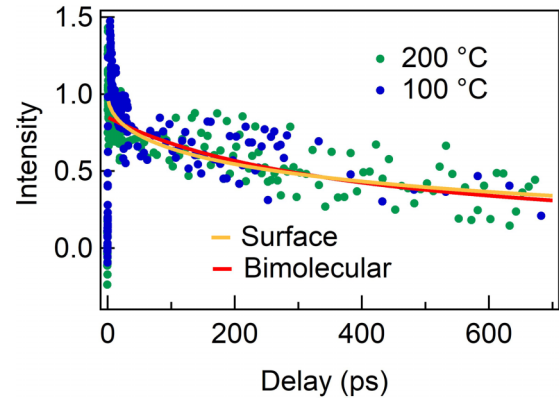


FIG. 8. Temporal evolution of the integrated 2PPE signal in the sample annealed at 100 °C (blue marks) and 200 °C (green marks). The red line is a fitting curve with bimolecular recombination rate $\gamma = 4 \pm 1 \times 10^{-10} \text{ cm}^3/\text{s}$ whereas the yellow line (which is almost indistinguishable from the red line) is the fit obtained by Eq. (2) with $S = 4000 \text{ cm/s}$ and $D_T = 0.05 \text{ cm}^2/\text{s}$.

where D_T is the diffusion constant of trapped electrons and S is the velocity of surface recombination. Figure 8 compares the long-time-scale dynamics measured in the MA100 and MA200 crystals with the fit obtained for $S = 4000 \text{ cm/s}$ and $D_T = 0.05 \text{ cm}^2/\text{s}$. Such S value is strictly an upper bound because (i) we chose the D_T value that provides a good fit and maximize S , and (ii) the model of Eq. (2) neglects the bimolecular recombination. The upper bound of S is not far from the surface recombination velocity estimated in other hybrid perovskites [27,34]. It should be outlined that $S < 4000 \text{ cm/s}$ is two or three orders of magnitude lower than the surface recombination velocity of most unpassivated semiconductors [35,36]. Accordingly, the electronic structure calculations do not predict midgap states at MaPbI_3 surfaces with thermodynamical stability [37]. In operating devices, this asset favors the efficient extraction or injection of carriers at the electrical contacts with the MAPbI_3 layer.

VIII. CONCLUSIONS

To conclude, we characterized the dynamics of excited electrons at the surface of MAPbI_3 . Our data provide a direct visualization of the electronic cooling at early delay times. It follows that photoexcited carriers thermalize on a subpicosecond time scale, presumably because of the coupling to the vibrations of organic cations. In the as-grown crystal, the electron dynamics is ruled by diffusion at long time scales. Most likely, an additional drift due to built-in fields sets in at early delay.

We intentionally induce compositional disorder in some MAPbI_3 crystals by thermal annealing in atmospheric conditions. As a result, the photoexcited electrons are localized by shallow traps within a few picoseconds. Such localization mechanism is consistent with the drop of photoconversion efficiency in aged cells. Finally we estimate the surface recombination velocity of MAPbI_3 cleaved in ultrahigh vacuum. The upper bound obtained by our analysis is consistent with previous results and is several orders of magnitude lower than the values reported in many unpassivated semiconductors.

ACKNOWLEDGMENTS

The project leading to this article has received funding from the European Union's Horizon 2020 research and innovation

program under Grant Agreement No. 687008 (GOTSolar). We also thank dim-nanoK for funding under the project "PIED" and DIM-Oximore and the Ecole Polytechnique for funding under the project "ECOGAN."

-
- [1] H. Zhou, Q. Chen, G. Li, S. Luo, T.-B. Song, H.-S. Duan, Z. Hong, J. You, Y. Liu, and Yang Yang, *Science* **345**, 542 (2014).
- [2] W. S. Yang, J. H. Noh, N. J. Jeon, Y. C. Kim, S. Ryu, J. Seo, and S. I. Seok, *Science* **348**, 1234 (2015).
- [3] M. A. Green, K. Emery, Y. Hishikawa, W. Warta, and E. D. Dunlop, *Prog. Photovoltaics* **24**, 905 (2016).
- [4] E. I. Wei, R. S. Xingang, C. Luzhou, and C. H. Choy Wallace, *Appl. Phys. Lett.* **106**, 221104 (2015).
- [5] T. M. Brenner, D. A. Egger, L. Kronik, G. Hodes, and D. Cahen, *Nat. Rev. Mater.* **1**, 15007 (2016).
- [6] Q. Dong, Y. Fang, Y. Shao, P. Mulligan, J. Qiu, L. Cao, and J. Huang, *Science* **347**, 967 (2015).
- [7] D. A. Valverde-Chavez, C. S. Ponseca, C. C. Stoumpos, A. Yartsev, M. G. Kanatzidis, V. Sundström, and D. G. Cooke, *Energy Environ. Sci.* **8**, 3700 (2015).
- [8] W. Tian, C. Zhao, J. Leng, R. Cui, and S. Jin, *J. Am. Chem. Soc.* **137**, 12458 (2015).
- [9] C. S. Ponseca, T. J. Savenije, M. Abdellah, K. Zheng, A. Yartsev, T. Pascher, T. Harlang, P. Chabera, T. Pullerits, A. Stepanov, J.-P. Wolf, and V. Sundström, *J. Am. Chem. Soc.* **136**, 5189 (2014).
- [10] C. Wehrenfennig, G. E. Eperon, M. B. Johnston, H. J. Snaith, and L. M. Herz, *Adv. Mater.* **26**, 1584 (2014).
- [11] P. T. Films, R. L. Milot, G. E. Eperon, H. J. Snaith, M. B. Johnston, and L. M. Herz, *Adv. Funct. Mater.* **25**, 6218 (2015).
- [12] K. Jemli, H. Diab, F. Lédée, G. Trippé-Allard, D. Garrot, B. Geffroy, J.-S. Lauret, P. Audebert, and E. Deleporte, *Molecules* **21**, 885 (2016).
- [13] M.-I. Lee, A. Barragán, M. N. Nair, V. L. R. Jacques, D. Le Bolloch, P. Fertey, K. Jemli, F. Lédée, G. Trippé-Allard, E. Deleporte, A. Taleb-Ibrahimi, and A. Tejada, *J. Phys. D: Appl. Phys.* **50**, 26LT02 (2017).
- [14] H. Diab, G. Trippé-Allard, F. Lédée, K. Jemli, C. Vilar, G. Bouchez, V. L. R. Jacques, A. Tejada, J. Even, J.-S. Lauret, E. Deleporte, and D. Garrot, *J. Phys. Chem. Lett.* **7**, 5093 (2016).
- [15] J. Faure, J. Mauchain, E. Papalazarou, W. Yan, J. Pinon, M. Marsi, and L. Perfetti, *Rev. Sci. Instrum.* **83**, 043109 (2012).
- [16] M. A. Green, Y. Jiang, A. M. Soufiani, and A. Ho-Baillie, *J. Phys. Chem. Lett.* **6**, 4774 (2015).
- [17] A. A. Ünal, A. Winkelmann, C. Tusche, F. Bisio, M. Ellguth, C. T. Chiang, J. Henk, and J. Kirschner, *Phys. Rev. B* **86**, 125447 (2012).
- [18] M. R. Filip, C. Verdi, and F. Giustino, *J. Phys. Chem. C* **119**, 25209 (2015).
- [19] D. Daniel Niesner, H. Zhu, K. Miyata, P. P. Joshi, T. J. S. Evans, B. J. Kudisch, M. Tuan Trinh, M. Marks, and X.-Y. Zhu, *J. Am. Chem. Soc.* **138**, 15717 (2016).
- [20] H. Tanimura, J. Kanasaki, K. Tanimura, J. Sjakste, N. Vast, M. Calandra, and F. Mauri, *Phys. Rev. B* **93**, 161203(R) (2016).
- [21] F. Brivio, J. M. Frost, J. M. Skelton, A. J. Jackson, O. J. Weber, M. T. Weller, A. R. Goni, A. M. A. Leguy, P. R. F. Barnes, and A. Walsh, *Phys. Rev. B* **92**, 144308 (2015).
- [22] D. B. Straus, S. H. Parra, N. Iotov, J. Gebhardt, A. M. Rappe, J. E. Subotnik, J. M. Kikkawa, and C. R. Kagan, *J. Am. Chem. Soc.* **138**, 13798 (2016).
- [23] Ye Yang, D. P. Ostrowski, R. M. France, K. Zhu, Jao van de Lagemaat, J. M. Luther, and M. C. Beard, *Nat. Photonics* **10**, 53 (2016).
- [24] M. B. Price, J. Butkus, T. C. Jellicoe, A. Sadhanala, A. Briane, J. E. Halpert, K. Broch, J. M. Hodgkiss, R. H. Friend, and F. Deschler, *Nat. Commun.* **6**, 8420 (2015).
- [25] H. Yan, D. Song, K. F. Mak, I. Chatzakis, J. Maultzsch, and T. F. Heinz, *Phys. Rev. B* **80**, 121403(R) (2009).
- [26] H. Zhu, K. Miyata, Y. Fu, J. Wang, P. P. Joshi, D. Niesner, K. W. Williams, S. Jin, and X.-Y. Zhu, *Science* **353**, 1409 (2016).
- [27] Ye Yang, Y. Yan, M. Yang, S. Choi, K. Zhu, J. M. Luther, and M. C. Beard, *Nat. Commun.* **6**, 7961 (2015).
- [28] M. Hajlaoui, E. Papalazarou, J. Mauchain, L. Perfetti, A. Taleb-Ibrahimi, F. Navarin, M. Monteverde, P. Auban-Senzier, C. R. Pasquier, N. Moisan, D. Boschetto, M. Neupane, M. Z. Hasan, T. Durakiewicz, Z. Jiang, Y. Xu, I. Miotkowski, Y. P. Chen, S. Jia, H. W. Ji, R. J. Cava, and M. Marsi, *Nat. Commun.* **5**, 3003 (2014).
- [29] L. She, M. Liu, and D. Zhong, *ACS Nano* **10**, 1126 (2016).
- [30] H. Xie, X. Liu, L. Lyu, D. Niu, Q. Wang, J. Huang, and Y. Gao, *J. Phys. Chem. C* **120**, 215 (2016).
- [31] I. Deretzi, A. Alberti, G. Pellegrino, E. Smecca, F. Giannazzo, N. Sakai, T. Miyasaka, and A. La Magna, *Appl. Phys. Lett.* **106**, 131904 (2015).
- [32] T. Umebayashi, K. Asai, T. Kondo, and A. Nakao, *Phys. Rev. B* **67**, 155405 (2003).
- [33] C. A. Hoffman, K. Jarasiunas, H. J. Gerritsen, and A. V. Nurmikko, *Appl. Phys. Lett.* **33**, 536 (1978).
- [34] B. Wu, H. T. Nguyen, Z. Ku, G. Han, D. Giovanni, N. Mathews, H. J. Fan, and T. C. Sum, *Adv. Energy Mater.* **6**, 1600551 (2016).
- [35] M. C. Beard, G. M. Turner, and C. A. Schmuttenmaer, *Phys. Rev. B* **62**, 15764 (2000).
- [36] A. J. Sabbah and D. M. Riffe, *J. Appl. Phys.* **88**, 6954 (2000).
- [37] J. Haruyama, K. Sodeyama, L. Han, and Y. Tateyama, *J. Phys. Chem. Lett.* **5**, 2903 (2014).